



A stable Ag₃PO₄@PANI core@shell hybrid: Enrichment photocatalytic degradation with π-π conjugation

Li Liu, Lan Ding, Yongguang Liu, Weijia An, Shuanglong Lin, Yinghua Liang, Wenquan Cui*

College of Chemical Engineering, Hebei Key Laboratory for Environment Photocatalytic and Electrocatalytic Materials, North China University of Science and Technology, Tangshan 063009, PR China

ARTICLE INFO

Article history:

Received 8 June 2016

Received in revised form 31 July 2016

Accepted 2 August 2016

Available online 3 August 2016

Keywords:

Ag₃PO₄@PANI

Core@shell structure

π-π Conjugation

Photocatalysis degradation

Stability

ABSTRACT

Here we report an Ag₃PO₄@PANI visible photocatalyst with core@shell structure prepared by a chemisorption method. The photocatalytic activity of Ag₃PO₄@PANI was enhanced significantly with increasing proportion of PANI. The high photocatalytic performance for the degradation of phenol and 2,4-dichlorophenol over Ag₃PO₄@PANI (5 wt %) composite photocatalyst reached 100% and 95.3%, which were 1.44 and 1.38 times of that of bulk Ag₃PO₄, respectively. The photocatalytic activity of Ag₃PO₄@PANI remained 85% after five cycling runs, whereas the activities of M-Ag₃PO₄/PANI (5 wt %) and Ag₃PO₄ remained 42% and 24%, respectively, indicating that Ag₃PO₄@PANI photocatalyst possessed a superior stability. Further analyses showed that the enhancement of photocatalytic activity and photo-stability originated from the superior charge mobility derived from the π-conjugated structure of PANI and the hybridization effect arising from Ag₃PO₄ and PANI. Moreover, the matched energy level between PANI and Ag₃PO₄ led to the efficient separation and transfer of photo-generated electron-hole at their interface, thus improving the photocatalytic performance of Ag₃PO₄@PANI composite. In addition, PANI shell can prevent the dissolution of Ag₃PO₄ particles in aqueous solution during the photocatalytic reaction, resulting in a high stability of the Ag₃PO₄@PANI composite photocatalyst.

© 2016 Elsevier B.V. All rights reserved.

1. Introduction

Photocatalysts, especially those with high photocatalytic activity and strong stability under visible light, have been regarded as promising materials for applications in solar energy conversion and treatment of water pollution [1,2]. Although TiO₂ is the most investigated photocatalyst so far [3], the wide energy gap (3.2 eV) of TiO₂ has hindered its sufficient utilization of sunlight [4,5]. Therefore, the development of novel and more efficient visible-light-driven (VLD) photocatalysts is still urgently needed from the viewpoint of solar energy utilization.

Ag₃PO₄ based photocatalysts have attracted considerable attention because of their excellent visible-light-driven photocatalytic activities for the degradation of organic pollutants and a broad band gap of 2.45 eV [6]. As a photocatalyst, Ag₃PO₄ has an indirect band gap and photo-excited holes with strong oxidation capability in the VB, and the mobility of the electron is significantly higher than that

of the hole. This facilitates the separation of electron-hole pairs partially because of the formation of the delocalized π* antibonding states in the CB. In addition, the inductive effect of PO₄³⁻ facilitates the e⁻/h⁺ separation, which considerably contributes to its excellent photocatalytic activity [7]. Ye and co-workers [8] discovered that Ag₃PO₄ possessed extremely high photo-oxidative capabilities for O₂ evolution from water as well as for organic dye degradation under visible light irradiation with a quantum efficiency of 90% at wavelengths greater than 520 nm, which is dozens of times higher than those of traditional photocatalytic materials TiO_{2-x}N_x, thus illustrating that Ag₃PO₄ has a tremendous potential for applications in photocatalytic materials. More interestingly, it has been recently revealed that uniform colloidal Ag₃PO₄ nanocrystals with a precise control of particle size ranging from 8 to 16 nm showed higher catalytic activity in the photodecomposition of MB under visible light irradiation than traditional photocatalysts, such as N-doped TiO₂-P25 and TiO₂-P25 [9]. However, the practical application of Ag₃PO₄ is severely limited by some drawbacks, including the severe photo-corrosion in photocatalysis process, which restricts the recycle and efficiency of the Ag₃PO₄ composite photocatalysts [10,11]. In addition, Ag₃PO₄ photocatalyst could slightly dissolve as Ag⁺

* Corresponding author.

E-mail address: wkcui@163.com (W. Cui).

and PO_4^{3-} in aqueous solution, thus reducing the photocatalytic activity and stability of Ag_3PO_4 . These adverse effects could be alleviated by blend with Fe_2O_3 [12], AgI [13] and ZnO [14] that could accelerate the photo-induced charge separation.

Photocatalysts with core@shell structures possess excellent visible-light-driven photocatalytic activity and many other advantages [15–17]. The stabilized material sheets coated on the surface of Ag_3PO_4 particles can prevent the dissolution of Ag_3PO_4 in aqueous solution, thus enhancing the structural stability of Ag_3PO_4 -based core@shell photocatalysts during the photocatalytic reaction [18]. The large contact area between core and shell can facilitate the separation of the photo-generated charge carriers at their interface. In addition, the coupling of Ag_3PO_4 with semiconductors can form a strong electric field at the interface near the band-edge offset, which can significantly accelerate the transfer of photo-generated charge carriers. Therefore, the shell materials that can facilitate the charge transfer and separation are strongly desired. To date, Ag_3PO_4 -based core-shell materials, such as BiPO_4 [19] and AgBr [20], generally exhibit point contact between the bulk phases, which lead to a weak conjunction of Ag_3PO_4 with semiconductors and could significantly limit the photo-induced charge separation. Therefore, there is the need to continue to explore novel core-shell materials for improving the activity and stability of Ag_3PO_4 photocatalyst.

Nowadays, delocalized π - π conjugated structures have been proven to induce a rapid photo-induced charge separation and to decrease the charge recombination rate in electron-transfer processes [21–23]. Recently, many research teams have developed some hybrid semiconductors from delocalized conjugative π structure materials as efficient photocatalysts, such as graphene [24], carbon nitride [25], and conductive polyaniline (PANI) [26]. In these studies, the delocalized conjugated materials closely matched with the photocatalysts in energy level, and an intensive interface hybrid effect emerged between conjugated materials, resulting in rapid charge separation and slow charge recombination in the electron-transfer process. Previously, our group reported that conjugative π structure of $\text{g-C}_3\text{N}_4$ nano-sheets coated on the surface of Ag_3PO_4 particles with core@shell structure can significantly enhance the photocatalytic activity and stability [27]. Polyaniline (PANI) is one of the conductive polymers having a delocalized π - π conjugated structure, in which the benzenoid and quinonoid units have several redox states with many other interesting properties [28]. Moreover, PANI is a promising candidate for large-scale applications due to its high conductivity, superior environmental stability, and convenient preparation. The combination of PANI with semiconductor improved the migration efficiency of charge carriers at the interface between PANI and semiconductor because of the superior charge carrier mobility of PANI, thereby facilitating the separation of photo-generated charge carriers and enhancing the photoelectrocatalytic performance. Zhu et al. [29] reported that the hybridization with monolayer PANI not only enhanced the photocatalytic activity but also remarkably inhibited the photo-corrosion of ZnO . Similarly, Wang et al. [30] prepared PANI@CdS core-shell nano-spheres by a proton doped in-situ polymerization method and demonstrated that the PANI@CdS substantially enhanced photocatalytic hydrogen production and photo-corrosion inhibition.

Herein, we reported a novel stable Ag_3PO_4 @PANI core@shell composite photocatalyst by a chemisorption method. Our result demonstrated the shell PANI could prevent the dissolution of Ag_3PO_4 in aqueous solution, thus enhancing the structural stability of Ag_3PO_4 . Meanwhile, the π - π conjugation in the structure of PANI and a strong interaction in the intimate contact interface resulted in an ultrafast conductivity, which efficiently facilitated the migration of interfacial charge carriers and the separation of photo-generated electrons and holes. This synergistic effect led to the suppression

of photo-corrosion of Ag_3PO_4 and generation of dramatic visible photocatalytic activity and photo-stability. The Ag_3PO_4 @PANI (5 wt.%) composite exhibited higher visible light photocatalytic degradation activity and stability than bare Ag_3PO_4 particles. The deep photo-oxidation activities for the degradation of phenol and 2,4-dichlorophenol over Ag_3PO_4 @PANI(5 wt.%) composite photocatalyst reached 100% and 95.3%, which were respectively 1.4 and 1.7 times of that of bulk Ag_3PO_4 .

2. Experimental

2.1. Synthesis of Ag_3PO_4

Ag_3PO_4 was prepared by a precipitation method. Briefly, 0.8 g PVP was suspended in 40 mL distilled water, followed by the addition of 0.8 g AgNO_3 . Na_2HPO_4 solution was prepared by dissolving 0.288 g Na_2HPO_4 in 20 mL distilled water and added to the PVP- AgNO_3 aqueous solution dropwise under stirring. The mixed solution was stirred for 1 h and centrifuged. The precipitate was collected, washed with water and ethanol for three times and dried at 60 °C for 12 h.

2.2. Synthesis of core@shell Ag_3PO_4 @PANI

The Ag_3PO_4 @PANI photocatalysts were fabricated as follows: a certain amount of Ag_3PO_4 powder was added to 100 mL of 0.45 g/L PANI (THF) solution with sonication for 30 min, and then the mixture was stirred for 48 h. The nominal weight ratios of PANI to Ag_3PO_4 were 1, 2, 5, 10, 15, and 20 wt.%, and the weights of Ag_3PO_4 were 1.2 g, 0.24 g, 0.17 g, 0.13 g and 0.12 g, respectively. After evaporation of water, the resulting residue was dried at 60 °C for 24 h to afford an Ag_3PO_4 @PANI composite powder. The sample named M- Ag_3PO_4 /PANI (5 wt.%) was prepared by the direct mechanical mixing of Ag_3PO_4 and PANI (5 wt.%) in an agate mortar.

2.3. Characterization of photocatalysts

The crystal structures and phase states of Ag_3PO_4 @PANI composites were determined by X-ray diffractometry (XRD) using a Rigaku D/MAX2500 PC diffractometer with $\text{Cu K}\alpha$ radiation at an operating voltage of 40 kV and an operating current of 100 mA. The morphologies of the samples were imaged with a scanning electron microscopy (SEM) (Hitachi, s-4800) and a transmission electron microscopy (TEM) (JEOL Ltd., JEM-2010). UV-vis (UV-vis) diffuse reflectance spectra were recorded on a UV-vis spectrometer (Puxi, UV1901). The band gap energies were calculated from a plot $(\alpha h\nu)^{1/2}$ vs. photo-energy ($h\nu$) using the Kubelka-Munk function which shows the relationship of band gap E_g and absorption coefficient α . The equation is as follows: $\alpha h\nu = A(h\nu - E_g)^{1/2}$. Where α is the absorption coefficient, ν is the frequency of the light, and h is Planck's constant. The Fourier transform infrared spectra (FTIR) of the samples were recorded on an IR Vertex70 FTIR spectrometer. Raman spectra were recorded on a microscopic confocal Raman spectrometer (Thermo Electron DXR) with an excitation of 785 nm laser light. Chemical states of these photocatalysts were analyzed with X-ray photoelectron spectroscopy (XPS) on an XSAM800 apparatus. Electrochemical and photo electrochemical measurements were performed in 0.1 M Na_2SO_4 electrolyte solution in a three-electrode quartz cell. Pt sheet was used as a counter electrode, and $\text{Hg}/\text{Hg}_2\text{Cl}_2/\text{sat. KCl}$ was used as a reference electrode. The Ag_3PO_4 @PANI composite thin film on an indium-tin oxide (ITO) was used as the working electrode for investigation. The photo electrochemical response was recorded with a CHI 660 B electrochemical system. The Ag^+ concentration in the solution was determined by Inductively Coupled Plasma (ICP) (HORIBA, ULTIMA2). To study the

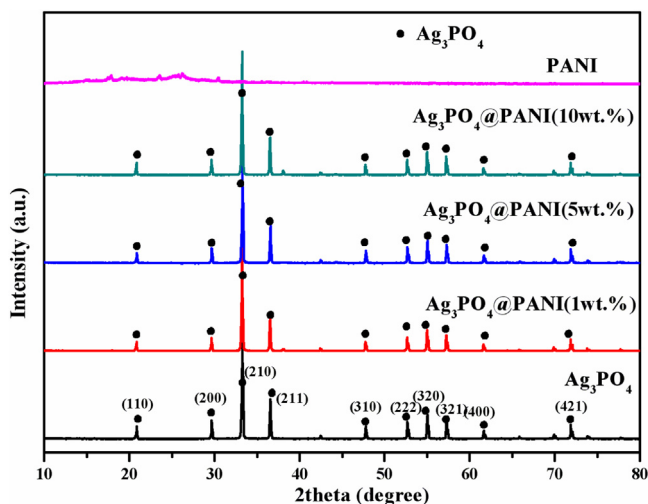


Fig. 1. XRD patterns of PANI, Ag_3PO_4 , and $\text{Ag}_3\text{PO}_4@\text{PANI}$ photocatalysts.

recombination of photo induced charge carrier, photoluminescence (PL, Hitachi F-7000, 250 nm) were measured.

2.4. Photocatalytic activity

The photocatalytic activities of the as-prepared samples were evaluated by the degradation of phenol solution in a multi-tube agitated reactor (XPA-7). The photocatalytic activity of $\text{Ag}_3\text{PO}_4@\text{PANI}$ composite was evaluated by catalytic degradation of phenol under visible light irradiation. A 250 W halide lamp (Royal Philips, Amsterdam, The Netherlands, flux is 17500 lm) with a 420 nm cutoff filter was used at a distance of 10 cm from an unsealed beaker. A glass reactor with $25 \pm 2^\circ\text{C}$ external circulating water was employed for the test group. 0.05 g photocatalyst was added to 50 mL of 10 mg/L phenol solution. Before the light irradiation, the suspensions were magnetically stirred for 30 min to reach the adsorption-desorption equilibrium. At given time interval, 3 mL aliquots were sampled and filtered with a micro-pore membrane. Simultaneously, the filtrates of phenol solutions at different conditions were analyzed by recording variations of the phenol peak area. HPLC was adopted for analysis of phenol concentration and the distribution of its degradation products. The mobile phase was composed of methanol and water (volume ratio: 60/40), and the elution time was 6 min at a flow rate of 1 mL/min. The detector was set at the wavelength of 270 nm, and C18 reversed phase column (Agilent 1100, 4.6 nm \times 200 nm) was used for chromatographic analysis. The conditions for the degradation of 2, 4-dichlorophenol were similar to those of phenol under visible light irradiation.

3. Results and discussion

The XRD measurements were carried out to determine the crystalline structure of PANI, Ag_3PO_4 , and $\text{Ag}_3\text{PO}_4@\text{PANI}$ composites (Fig. 1). In the case of the bare Ag_3PO_4 , all of the diffraction peaks could be clearly indexed to the cubic phase of Ag_3PO_4 (JCPDS card No. 06-0505). This phase could be characterized by the appearance of Bragg diffraction peaks at $2\theta = 20.9^\circ, 29.7^\circ, 33.3^\circ, 36.6^\circ, 47.8^\circ, 52.7^\circ, 55.0^\circ, 57.3^\circ, 61.6^\circ$ and 71.9° , which were indexed to (110), (200), (210), (211), (310), (222), (320), (321), (400) and (421) planes for Ag_3PO_4 , respectively. Compared with bare Ag_3PO_4 , the XRD patterns of core@shell structure $\text{Ag}_3\text{PO}_4@\text{PANI}$ did not vary in peaks or shapes. This finding indicated that coating on the PANI shell did not effect on the crystal structure of Ag_3PO_4 . Moreover, no characteristic diffraction peaks of PANI were detected in $\text{Ag}_3\text{PO}_4@\text{PANI}$

composite because PANI is amorphous in the composite photocatalyst [31].

The morphologies and microstructures of the as-prepared samples were studied by SEM and TEM, as shown in Fig. 2. Fig. 2a shows the SEM image of the pure Ag_3PO_4 . It could be seen that the Ag_3PO_4 particles were uniform in size with the estimated average diameter ranging from 200 to 300 nm. Fig. 2b is the high-magnification SEM image of the $\text{Ag}_3\text{PO}_4@\text{PANI}$ core@shell composite. It can be seen clearly that the PANI shell was uniformly coated on the surface of Ag_3PO_4 particles. Fig. 2c shows the TEM image of the pure Ag_3PO_4 . In Fig. 2c, the estimated diameter of the spherical Ag_3PO_4 particles was in the range of 200–300 nm. The TEM images (Fig. 2d and e) of the composite showed that the outer layer of the as-prepared $\text{Ag}_3\text{PO}_4@\text{PANI}$ sample was distinctly different from the Ag_3PO_4 core. This result was further confirmed by the high-resolution TEM images in Fig. 2f. These Ag_3PO_4 particles were in intimate contact with the PANI, and the lattice fringes of Ag_3PO_4 can be clearly identified in Fig. 2f. The lattice fringes of particles exhibited a spacing of 0.27 nm, which is in agreement with the spacing of the (210) plane of Ag_3PO_4 and consistent with JCPDS card no. 06-0505 [32]. Compared with point contact structure of traditional composite materials, the core@shell three-dimensional structure of $\text{Ag}_3\text{PO}_4@\text{PANI}$ has a larger contact area, which can significantly promote photo-induced charge separation. The overall process for the fabrication of the core@shell structure of $\text{Ag}_3\text{PO}_4@\text{PANI}$ is shown in Fig. 2g. First, synthetic Ag_3PO_4 particles were prepared by the precipitation method. The as-prepared particles were added to PANI (THF) solution and stirred at room temperature. Subsequently, the core@shell structure of PANI and Ag_3PO_4 was formed by incubation of the PANI with Ag_3PO_4 particles for 24 h, which minimized the surface energy of $\text{Ag}_3\text{PO}_4@\text{PANI}$.

The optical properties of the as-prepared samples were investigated by UV-vis diffuse reflectance spectra, as shown in Fig. 3. The light absorption edge of pure Ag_3PO_4 was 520 nm, corresponding to a band gap (E_g) of 2.45 eV [33]. After combination with PANI, a slightly red shift of the band edge, as well as an enhanced visible light response, was observed. The $\text{Ag}_3\text{PO}_4@\text{PANI}$ composite showed significantly stronger light absorption than Ag_3PO_4 . The band gap energy of a semiconductor could be calculated by the Kubelka-Munke equation [34]. As shown in Fig. 3b, the transition bandgaps estimated from the onset of the curve edges were about 2.45, 2.38, 2.21, 2.29, 2.24, and 2.13 eV for Ag_3PO_4 , $\text{Ag}_3\text{PO}_4@\text{PANI}$ (1 wt.%), $\text{Ag}_3\text{PO}_4@\text{PANI}$ (5 wt.%), $\text{Ag}_3\text{PO}_4@\text{PANI}$ (10 wt.%), $\text{Ag}_3\text{PO}_4@\text{PANI}$ (15 wt.%), and $\text{Ag}_3\text{PO}_4@\text{PANI}$ (20 wt.%), respectively. The relatively narrow band-gap energy observed for $\text{Ag}_3\text{PO}_4@\text{PANI}$ is likely attributed to the strong interaction of the hybrid structure, which enables more efficient utilization of the solar spectrum. Furthermore, the formation of a conjugated structure between the π -conjugated structure of PANI and Ag_3PO_4 over a wide range facilitates the migration efficiency of photo-induced charges and suppresses the charge recombination, thus enhancing the photocatalytic performance of $\text{Ag}_3\text{PO}_4@\text{PANI}$.

The Fourier transform infrared spectrometry (FTIR) spectra of PANI, Ag_3PO_4 , and $\text{Ag}_3\text{PO}_4@\text{PANI}$ composite photo-catalyst are shown in Fig. 4. The bands at 1659 cm^{-1} and 1381 cm^{-1} were attributed to the stretching and bending of H–O of water adsorbed on the surface, respectively [35–37]. The water molecules and hydroxyl groups adsorbed on the Ag_3PO_4 surface can be converted to hydroxyl free radicals in the photocatalytic reaction for the oxidation of organic pollutants. The two peaks at 1010 cm^{-1} and 558 cm^{-1} in the FTIR spectrum of Ag_3PO_4 were assigned to the P–O stretching vibration in PO_4^{3-} . The formation of PO_4^{3-} -tetrahedral units with strong P–O bonds weakens the covalent nature of Ag–O bonds, inhibiting hybridization of Ag d with O p. This excludes the d character from the conduction-band minimum (CBM), leaving highly dispersive Ag s–Ag s hybrid bands

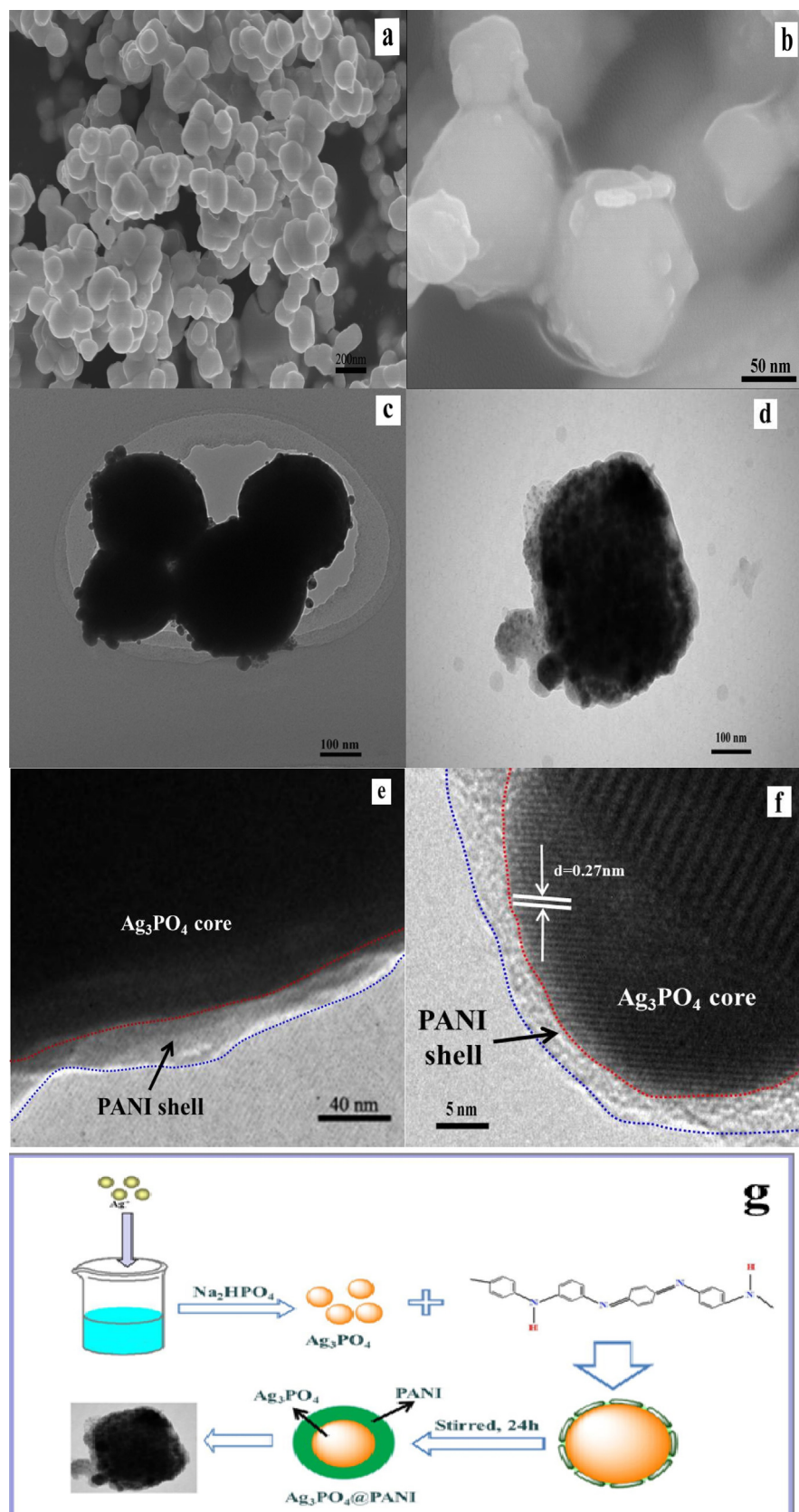


Fig. 2. SEM images of (a) Ag_3PO_4 , (b) Ag_3PO_4 @PANI, (c) TEM images of Ag_3PO_4 , (d, e) TEM images of Ag_3PO_4 @PANI, (f) HRTEM images of Ag_3PO_4 @PANI, (g) The schematic illustration of the preparation of Ag_3PO_4 @PANI composites.

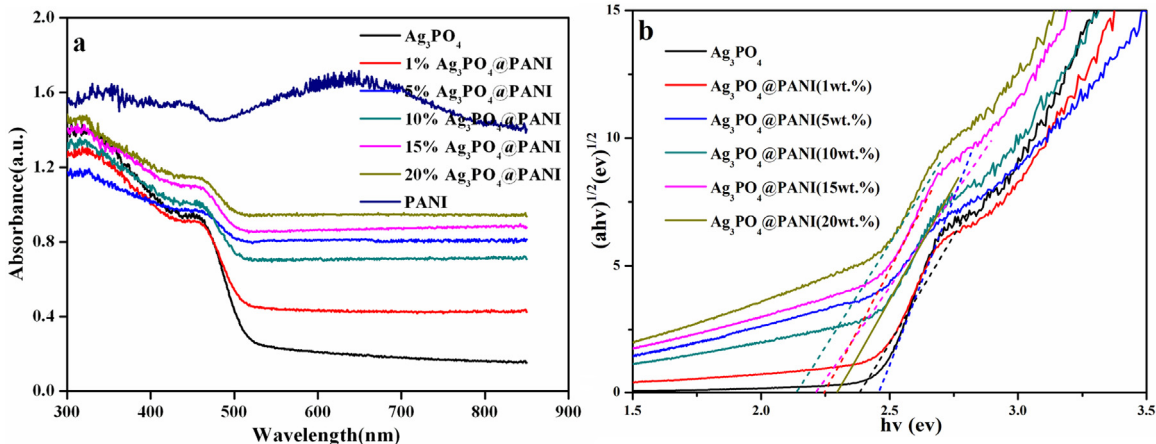


Fig. 3. (a) UV-vis diffuses reflectance spectra of the as-prepared Ag₃PO₄, PANI, and Ag₃PO₄@PANI. (b) Relationship of (ahv)^{1/2} vs. E (ev).

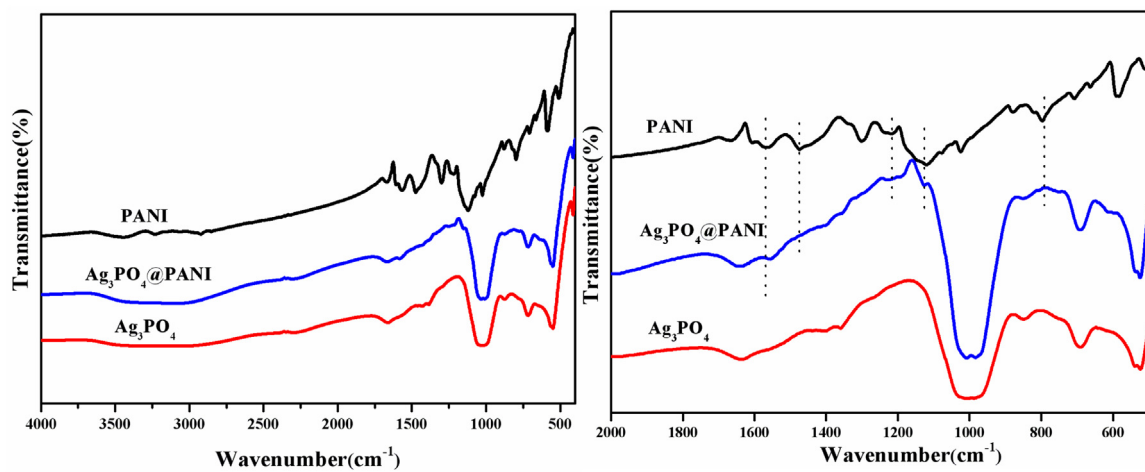


Fig. 4. FTIR spectra of Ag₃PO₄, PANI and Ag₃PO₄@PANI (5 wt.%).

[38]. The delocalized charge distribution of the CBM results in a small effective mass of the electron, which is favorable for the carrier transfer to the surface. The peaks of pure PANI at 1560 cm⁻¹ (C=N and C=C stretching modes) and 1294 cm⁻¹ (C–N stretching mode) shifted to lower wavenumbers [39], indicating that all of these chemical bonds were weakened. The red shift of these bands suggested that the bond strengths of C=N and C–N were reduced so that the PANI conjugated bond was stretched and a more conjugated structure containing PANI and Ag₃PO₄ was formed. A similar chemical bonding was also observed in the case of ZnO [29] and TiO₂ [40] hybrid monolayer polyaniline composite, as reported by Zhu et al. Compared with the point contact, the core@shell structure having a large contact area is more conducive to the formation of the interaction. This interaction is essential to promote the separation efficiency of photo-generated carriers and to enhance photocatalytic activity and anti-photocorrosion performance of Ag₃PO₄@PANI photocatalyst.

Raman spectroscopy analysis was further performed to confirm the interaction in the Ag₃PO₄@PANI composite. Fig. 5a shows the Raman spectra of Ag₃PO₄, PANI, and Ag₃PO₄@PANI composite. The strong absorption peak at 912 cm⁻¹ in the spectrum of Ag₃PO₄ can be assigned to the vibration of terminal oxygen bond of phosphate group [41]. The distinct Raman peak at 567 cm⁻¹ corresponded to the symmetric stretch of P–O–P bonds. For the Raman spectrum of PANI, the bands around 1596 cm⁻¹ were attributed to the vibrational mode of the benzenoid unit. A peak near 1476 cm⁻¹ was

assigned to the vibrational mode of the quinonoid unit, and the peak at about 1173 cm⁻¹ was the characteristic vibrational mode of the C–H bending [39]. In the Ag₃PO₄@PANI composite, all of these bands shifted to lower wavenumbers. The red shift of these bands suggested that the bond strengths of C=N (C=C) and C–N were weakened so that the PANI conjugated bond was stretched and a more conjugated structure containing PANI and Ag₃PO₄ was formed. On the basis of these results, it can be concluded that an intense interaction existed between PANI and Ag₃PO₄. The TG curves of Ag₃PO₄, PANI, and Ag₃PO₄@PANI (5 wt.%) are shown in Fig. 5b. It is evident that the thermal degradation of pure PANI consisted of two distinct stages. The first stage occurring from 100 to 300 °C was attributed to desorption of solvent, and the second stage extending from 350 to 800 °C was mainly caused by the chemical desorption and decomposition of PANI. The TG curves of Ag₃PO₄@PANI (5 wt.%) underwent a two-step weight loss pattern. The stage extending from 200 to 650 °C with a weight loss of 4.8% was attributed to the decomposition of PANI. The amount of weight loss was nearly equivalent to the amount of PANI (5.0%) coated on Ag₃PO₄. Moreover, the Ag₃PO₄@PANI (5 wt.%) sample hardly showed weight loss in the range of 100–300 °C, indicating a strong chemical interaction took place between Ag₃PO₄ and PANI. This strong chemical interaction limited the thermal motion of the polymer chain and increased the thermal degradation temperature, thereby enhancing the thermal stability of Ag₃PO₄ @ PANI composite [42].

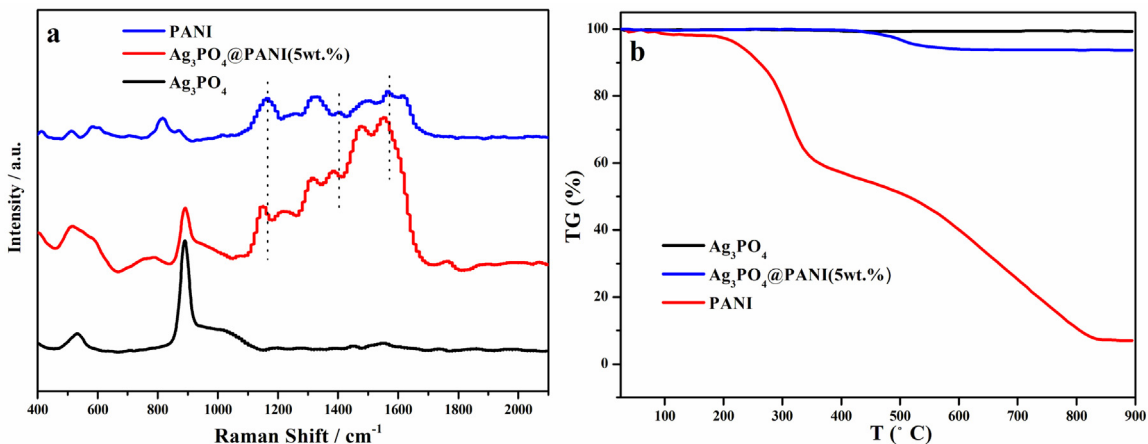


Fig. 5. (a) Raman spectra of Ag₃PO₄, PANI and Ag₃PO₄@PANI (5 wt.%), (b) TG curves of Ag₃PO₄, PANI and Ag₃PO₄@PANI (5 wt.%).

(XPS) analysis of Ag₃PO₄ and Ag₃PO₄@PANI was carried out to reveal more detail information about the interaction between PANI and Ag₃PO₄. Fig. 6a presents the survey spectra of Ag₃PO₄@PANI. The binding energies of typical three peaks of C 1s of Ag₃PO₄@PANI were at 284.2, 285.3, and 287 eV (Fig. 6b), corresponding to C—H or C=C, C—N, and C=N, respectively. The N 1s spectrum of Ag₃PO₄@PANI represented quinonoid diimine at 398.9 eV, benzenoid imine at 399.7 eV, and protonation imine at 400.8 eV. Moreover, an additional peak at 398.8 eV was observed, due to the formation of a new metal-N bond (Fig. 6c) [43]. The presence of M—NH⁺ indicated that there was a chemical interaction between the π-conjugated structure of Ag₃PO₄ and PANI, which resulted in a larger conjugated system in Ag₃PO₄@PANI composite. Compared with Ag₃PO₄, both the binding energies of Ag and P shifted slightly in Ag₃PO₄@PANI (Fig. 6d and e), indicating there was an intense interfacial interaction between Ag₃PO₄ and PANI [44]. The increased binding energy of surface atoms suggested that the Ag₃PO₄@PANI was more stable under visible-light irradiation than the pure Ag₃PO₄. Fig. 6f displays the Ag 3d level spectrum. For pure Ag₃PO₄, the Ag 3d3/2 and Ag 3d5/2 spin-orbital photoelectrons were located at binding energies of 373.99 eV and 367.94 eV, respectively. The Ag 3d3/2 peak was further divided into two different peaks at 373.8 and 374.15 eV, and the Ag 3d5/2 was also split into two distinct peaks at 367.89 and 368.4 eV. According to the report [45] by Zhang et al., the Ag 3d peaks with the binding energies of 373.8 and 367.89 eV corresponded to the Ag⁺. In addition, the peaks at 374.15 and 368.4 eV were attributed to metallic silver, and these two peaks with a spin energy separation of 6.1 eV further indicated that the Ag⁰ existed in the Ag₃PO₄ composite [46]. However, the peaks of Ag₃PO₄ @ PANI at 368.4 and 374.15 eV did not exhibit a split peak, indicating that the presence of Ag⁺ in the sample. These observations further confirmed that the incorporation of PANI into Ag₃PO₄ photocatalyst could substantially enhance the stability of Ag₃PO₄.

Transient photocurrent responses were determined to investigate the photoelectric responses of the photoelectrodes. As shown in Fig. 7a, the Ag₃PO₄@PANI (5 wt.%) produced a much higher photocurrent than both Ag₃PO₄ and PANI under same conditions. This indicated that the combination of Ag₃PO₄ and PANI was able to facilitate the photoinduced charge migration efficiently, which was a result of the hybridization effect in the Ag₃PO₄@PANI composite. From these results, it could be concluded that the highly enhanced photocurrent response of Ag₃PO₄@PANI is attributed to the superior charge mobility derived from the π-conjugation in the structure of PANI and to the formation of the new chemical bond between PANI and Ag₃PO₄. In general,

PL emission spectra are useful to reveal the efficiency of photo-generated carrier trapping, migration, transfer, separation, and recombination. Fig. 7b presents the PL emission spectra of Ag₃PO₄ and Ag₃PO₄@PANI composite. The luminous peak of these photocatalysts was observed at around 525 nm. Compared with pure Ag₃PO₄, the intensity of the Ag₃PO₄@PANI composite displayed a considerable decrease in fluorescence. The quenched fluorescence indicated an efficient separation of photo-generated electron-hole pairs, which resulted in enhanced photocatalytic degradation performance of Ag₃PO₄@PANI composite. Photoelectrochemical measurements were carried out to study the photoelectrocatalytic performance. EIS has been proven to be a significant tool for the investigation of the charge transfer process on the electrode and at the interfacial contact between the electrode and electrolyte. This method is generally used to probe the separation efficiency of photo-induced charges. Fig. 7c shows a typical EIS of the prepared samples. The equivalent circuit (inset in Fig. 7c) of the device was conducted to analyze further the impedance spectra, which were fitted using the ZSimpWin software. R₁ is the series resistance of the system. The first semi-circle (high frequency) can be assigned to the charge-transfer resistance (R₂) of the Pt counter electrode/electrolyte interface. The second semi-circle (middle frequency) can be assigned to the charge-transfer resistance (R₂) of the as-prepared sample anode/electrolyte interface. The R₃ represents the charge transfer resistance in Helmholtz layer, whereas CPE represents the chemical capacitance. Fig. 7c shows the semi-circular Nyquist plot. It clearly indicated that the diameter of the arc radius on the EIS Nyquist plot of the Ag₃PO₄@PANI (5 wt.%) composite electrode was much smaller than those of the Ag₃PO₄ and PANI electrodes under visible light irradiation, implying that the Ag₃PO₄@PANI photo-electrode exhibited the fastest interfacial charge transfer and the most efficient separation of photo-generated charge carriers compared with pure Ag₃PO₄ and PANI. Fig. 7d showed that the characteristic peak of the Ag₃PO₄@PANI photo-electrode shifted from 387.38 Hz to 31.19 Hz, compared with that of pure Ag₃PO₄. The shift of a peak from a high frequency to a low frequency indicated a more rapid electron transfer process because frequency (f) is closely related to the lifetime (τ) of the injected electrons according to the equation: $\tau \approx 1/(2\pi f)$. According to this equation, the electron lifetime of Ag₃PO₄@PANI (5.105 ms) was estimated to be 8.6 times higher than that of pure Ag₃PO₄ (0.411 ms), which indicated a higher injected electron lifetime and considerably inhibited charge recombination in the Ag₃PO₄ photo-electrode, resulting in enhanced charge separation efficiency and improved photoelectrocatalytic performance.

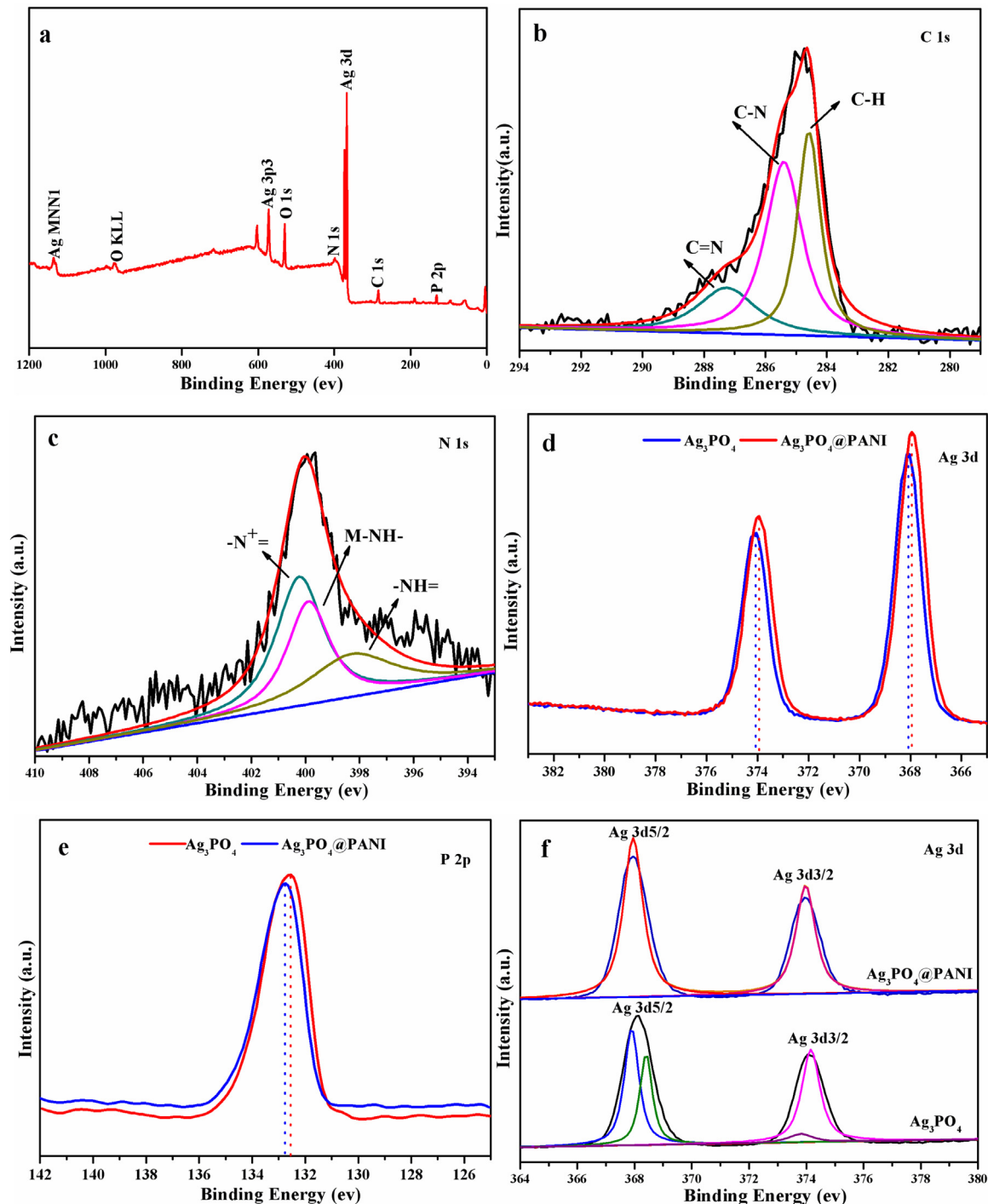


Fig. 6. The XPS spectra of Ag_3PO_4 and $\text{Ag}_3\text{PO}_4@\text{PANI}$ (5 wt.%): (a) survey spectra; (b) C 1s and (c) N 1s spectrum of $\text{Ag}_3\text{PO}_4@\text{PANI}$ (5 wt.%); (d)Ag 3d; (e)P 2p; (f)Ag 3d of Ag_3PO_4 and $\text{Ag}_3\text{PO}_4@\text{PANI}$ (5 wt.%), respectively.

The photocatalytic activities of different samples for the phenol degradation under the visible light are shown in Fig. 8. As shown in Fig. 8a, phenol was only slightly degraded in the absence of the catalyst or the presence of the catalyst in the dark, indicating that the blank photolytic degradation was negligible. In contrast, nearly 100% of phenol was degraded with 30 min irradiation in the presence of $\text{Ag}_3\text{PO}_4@\text{PANI}$ photocatalyst, which demonstrated the excellent photocatalytic activity of $\text{Ag}_3\text{PO}_4@\text{PANI}$. The photocatalyst prepared by simple mechanical mixing Ag_3PO_4 with PANI (5 wt.%) in an agate mortar only degraded 83% of phenol under the same conditions. Similarly, Only 69% phenol was degraded by pure

Ag_3PO_4 under visible light irradiation for 30 min. The phenol degradation in the presence of PANI was also investigated under the same conditions. It turned out that phenol was slightly degraded in the presence of PANI only. These results indicated that $\text{Ag}_3\text{PO}_4@\text{PANI}$ core@shell composite is a more efficient photocatalyst than pure Ag_3PO_4 , PANI, and $\text{M-Ag}_3\text{PO}_4/\text{PANI}$ (5 wt.%). Fig. 8b shows the HPLC chromatogram during the photo-degradation of phenol over $\text{Ag}_3\text{PO}_4@\text{PANI}$ (5 wt.%) under visible light irradiation. The phenol showed a characteristic peak with a retention time (RT) of 4.7 min [47]. The phenol peak became weaker with increasing irradiation time and disappeared completely after 30 min, indicating the excel-

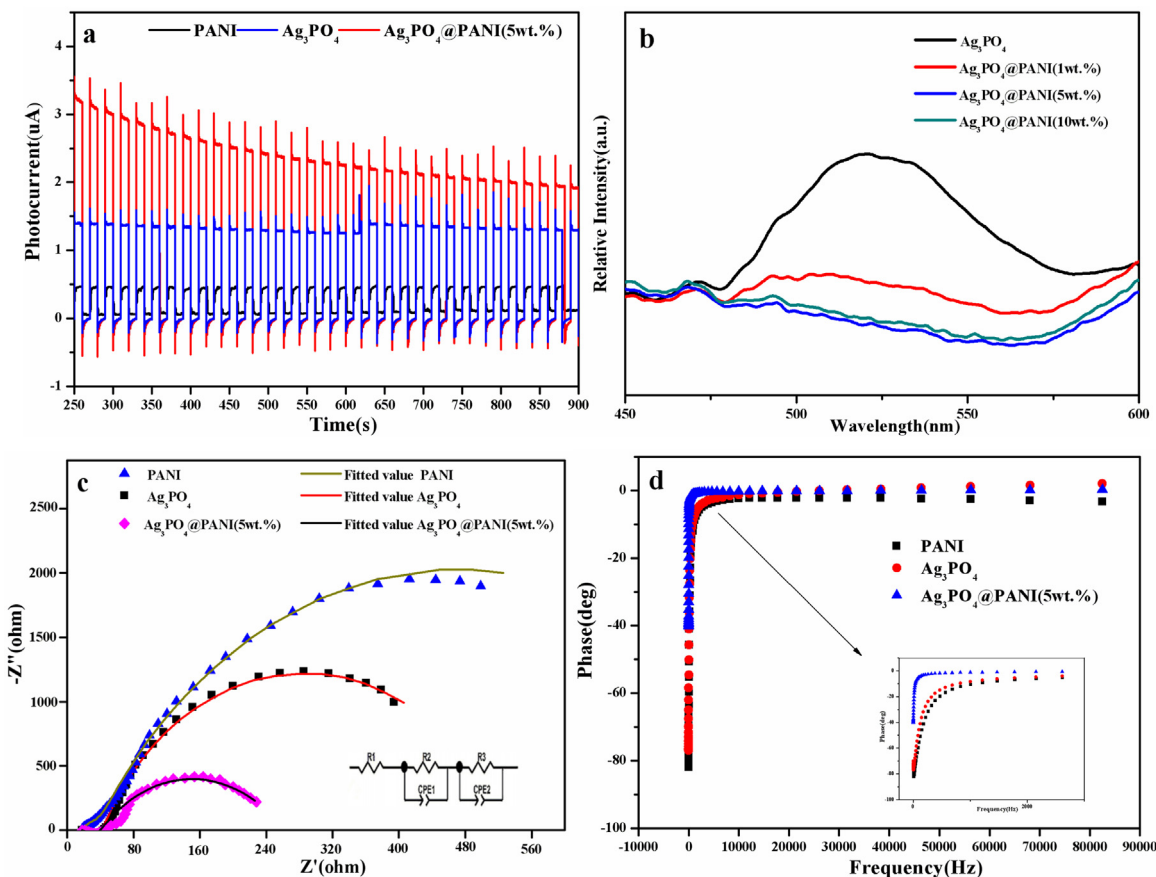


Fig. 7. (a) Transient photocurrent responses of pure Ag_3PO_4 , PANI, and $\text{Ag}_3\text{PO}_4@\text{PANI}$, (b) The photoluminescence spectra of the prepared Ag_3PO_4 , $\text{Ag}_3\text{PO}_4@\text{PANI}$, (c) EIS plots of the samples under irradiation with visible light. Inset: equivalent circuit used to fit the data, (d) the Bode-phase of pure Ag_3PO_4 , PANI, and $\text{Ag}_3\text{PO}_4@\text{PANI}$.

lent photocatalytic activity of $\text{Ag}_3\text{PO}_4@\text{PANI}$. Three-dimensional HPLC chromatographic analysis was conducted to further evaluate the photocatalytic activity of the $\text{Ag}_3\text{PO}_4@\text{PANI}$ (5 wt.%). The retention time and shape of peak reflected the degradation of phenol in solution. As shown in Fig. 8c, in the reaction time of 0 min, HPLC solvent peak and phenol corresponding peak were observed in the chromatogram. After 30 min illumination, only the HPLC solvent peak was observed in the chromatogram, and the peaks corresponding to phenol disappeared (Fig. 8d), demonstrating that phenol was degraded to CO_2 and H_2O in the process of photocatalytic reaction. To further elucidate the degradation products and degradation pathway of phenol in the presence of $\text{Ag}_3\text{PO}_4@\text{PANI}$, we conducted photocatalytic experiments with prolonged irradiation times (30 min). It was found that the as-prepared $\text{Ag}_3\text{PO}_4@\text{PANI}$ hybrid hydrogels exhibited enhanced performance in TOC removal of phenol solution. Fig. 8f shows the TOC removal of phenol as a function of reaction time. After 30 min illumination, the TOC removal by PANI, Ag_3PO_4 , $\text{Ag}_3\text{PO}_4@\text{PANI}$ (5 wt.%), M-5% $\text{Ag}_3\text{PO}_4/\text{PANI}$ were 4.67%, 51%, 78%, 61%, respectively. This further illustrated that the photocatalytic activity and mineralization ability of $\text{Ag}_3\text{PO}_4@\text{PANI}$ are obviously superior to other investigated catalysts.

Next, we investigated the effect of PANI content on the photocatalytic activity of $\text{Ag}_3\text{PO}_4@\text{PANI}$ composite. Fig. 9 shows degradation rate (a) and first-order rate constant (b) of $\text{Ag}_3\text{PO}_4@\text{PANI}$ composite. The photocatalytic performance significantly improved after the introduction of PANI and increased with the increase of PANI content from 1.0 to 5.0 wt.%. For example, the $\text{Ag}_3\text{PO}_4@\text{PANI}$ composite containing 5.0 wt.% PANI degraded 100% of phenol and exhibited a photodegraded rate constant of 0.2181 min^{-1} , rep-

resenting an optimal coating amount with a high photocatalytic activity. However, further increasing the PANI content to 20 wt.% in the composite led to a decrease in photocatalytic activity. It also could be seen from the graph of Fig. 9 that the coating amount of PANI significantly affected the photocatalytic activity of the as-prepared samples. When the PANI content was relatively low (<5.0 wt.%), the contact area gradually increased with the increment of PANI. Therefore, an effective charge separation can be achieved, resulting in enhancement of photocatalytic activity and inhibition of photo-corrosion. On the other hand, when the PANI content was relatively high (>5.0 wt.%), a significant amount of PANI formed a thick and completely closed shell on the Ag_3PO_4 particles, which suppressed the transfer of electrons on the enriched Ag_3PO_4 to the surface of PANI. Under the circumstance, it reduced the number of hydroxyl radical which can act as a dominant reactive species in the photocatalytic degradation. Simultaneously, this can facilitate the recombination of photoinduced electron-hole pairs. Consequently, the photocatalytic activity decreased rapidly with further increasing of the PANI content. These results demonstrated that the PANI shell could enhance the photocatalytic degradation activity, and proper thickness of PANI shell is critical for the enhancement of photocatalytic activity.

In the present work, the degradation of 2, 4-dichlorophenol over $\text{Ag}_3\text{PO}_4@\text{PANI}$ under visible light irradiation (>420 nm) was also studied for the assessment of the photocatalytic performance of $\text{Ag}_3\text{PO}_4@\text{PANI}$ composite. As can be seen from Fig. 10a, 2, 4-dichlorophenol was degraded with a degradation ratio of 68.6% over Ag_3PO_4 under visible light irradiation for 30 min. The degradation ratio significantly increased to 95.3% over the $\text{Ag}_3\text{PO}_4@\text{PANI}$ composite photocatalyst with a 30 min visible light irradiation.

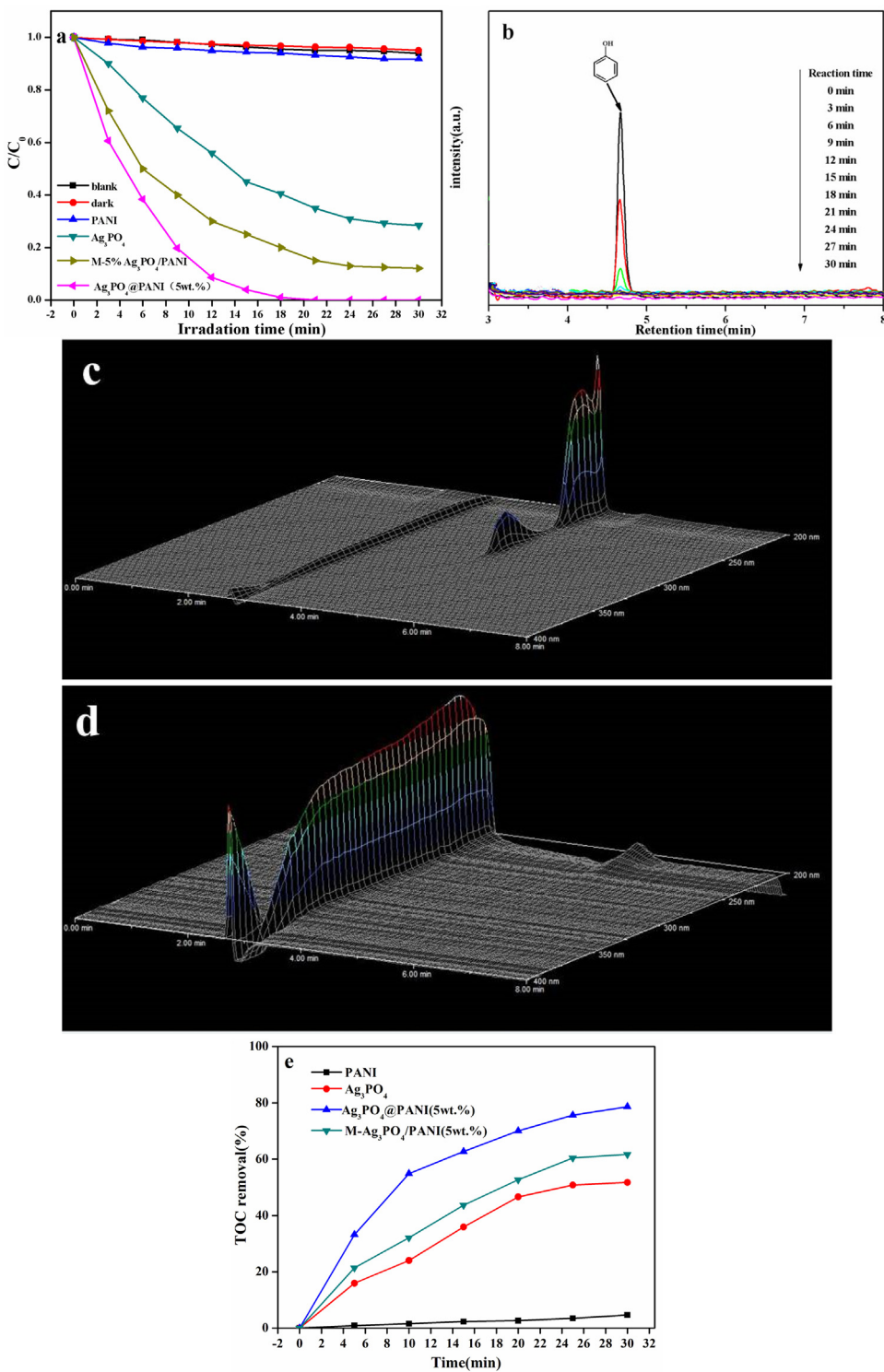


Fig. 8. (a) The variation of phenol concentration over various photocatalysts under visible light irradiation (b) HPLC chromatograms of phenol solutions with $\text{Ag}_3\text{PO}_4@\text{PANI}$ (5 wt.%) photocatalytic catalyst (c) Three-dimensional HPLC chromatographic spectra of phenol degradation (0 min) (d) Three-dimensional HPLC chromatographic spectra of phenol degradation (30 min) (e) TOC removal of phenol over various photocatalysts under visible light irradiation.

These results indicated that $\text{Ag}_3\text{PO}_4@\text{PANI}$ could also be used for the removal of 2, 4-dichlorophenol via photocatalytic degradation rather than physical adsorption. Well-aligned band-structure and the strong interaction in the intimate contact interface enhance the charge separation, which results in excellent photocatalytic activity. To obtain more information about intermediate species formed during the degradation process, we analyzed the degradation mixture by HPLC analysis. As shown in Fig. 10b, the 2,

4-dichlorophenol showed a characteristic peak with a retention time (RT) of 6.1 min. By comparison of the retention time with the reference standards under the same operating conditions, benzoquinone (RT = 3.6 min) and 2-chlorohydroquinone (RT = 3.8 min) were identified to be the main degradation intermediates of 2, 4-dichlorophenol in $\text{Ag}_3\text{PO}_4@\text{PANI}$ system [48,49]. As the reaction preceded, the peak intensity of both 2, 4-dichlorophenol and intermediate species decreased with continuous irradiation. Neither 2,

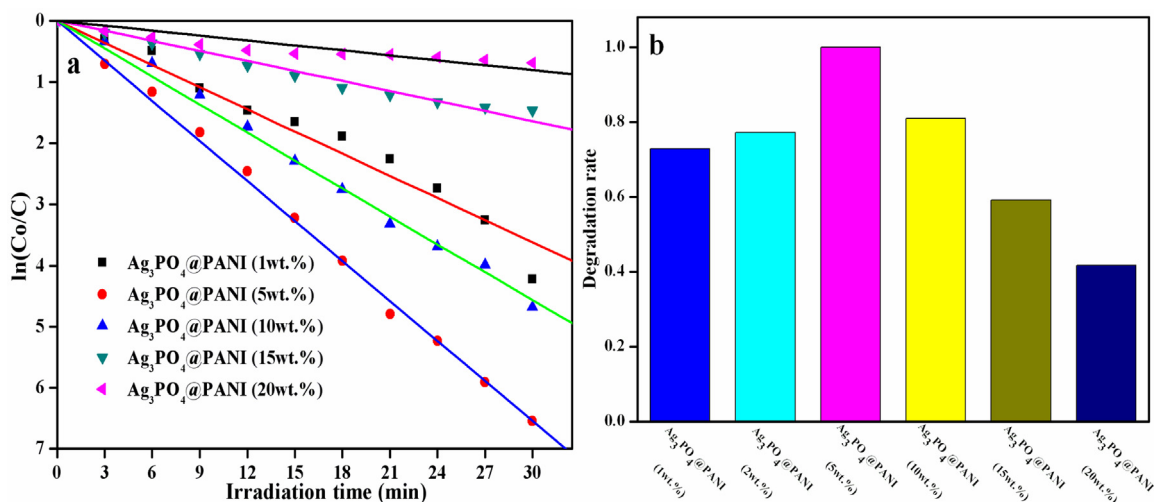


Fig. 9. Degradation rate (a) and first-order rate constant (b) of Ag_3PO_4 @PANI composite with various PANI contents on degradation of phenol.

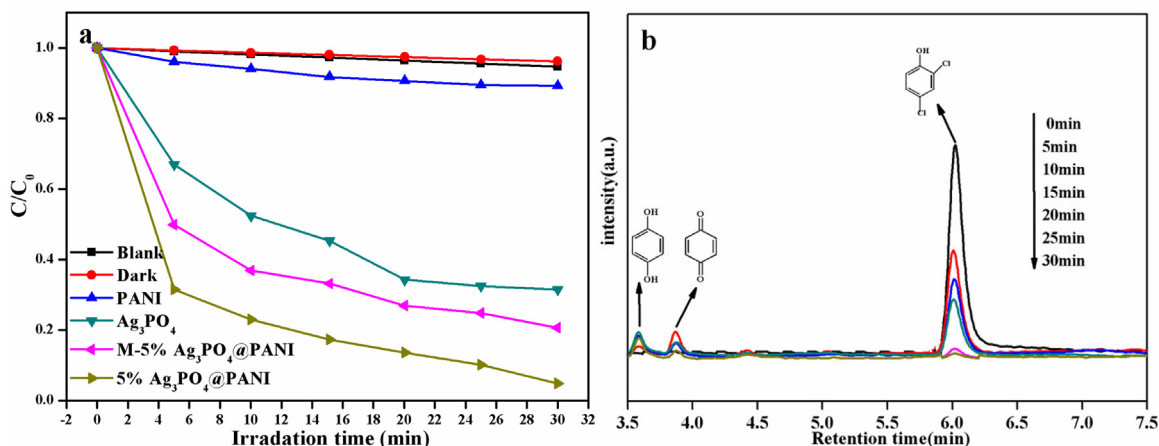


Fig. 10. (a) The variation of 2, 4-dichlorophenol concentration over various photocatalysts under visible light irradiation (b) Evolution of HPLC chromatograms for 2, 4-dichlorophenol solutions using Ag_3PO_4 @PANI (5%) catalyst.

4-dichlorophenol nor intermediate species was detected after irradiated for 30 min, which indicated that 2, 4-dichlorophenol was mineralized to CO_2 and H_2O completely.

To test the stability of the Ag_3PO_4 @PANI composite, we conducted a series of photostability experiments. Fig. 11a shows the photostability (phenol as a probe molecule) of Ag_3PO_4 , Ag_3PO_4 @PANI, M-5% Ag_3PO_4 /PANI composite. As shown in Fig. 11a, the degradation over bare Ag_3PO_4 decreased from 69% to 24% after five recycling runs. In contrast, 85% phenol was degraded over Ag_3PO_4 @PANI composite after five recycling runs, indicating it has a high stability in the photocatalytic reaction under visible light irradiation. To investigate the stability of the catalyst in the aqueous solution, we determined the amounts of Ag^+ from the dissolution of Ag_3PO_4 and Ag_3PO_4 @PANI in water under visible irradiation by using ICP. Ag_3PO_4 and Ag_3PO_4 @PANI (25 mg) were added to 100 mL of deionized water, and then 3 mL aliquots were sampled from the reactor at given intervals to analyze the concentrations of Ag^+ in the aqueous solution. As can be seen from Fig. 11b, the dissolution of Ag_3PO_4 in water proceeded rapidly during the reaction. When the visible light illumination time reached 100 h, the amount of Ag^+ in water was determined to be about 109.30 mg/g. In contrast, due to the slow dissolution of Ag_3PO_4 @PANI in water, the amount of Ag^+ solution of Ag_3PO_4 @PANI (1 wt.%), Ag_3PO_4 @PANI (5 wt.%), and Ag_3PO_4 @PANI (10 wt.%) were 60.23, 28.58, and 40.96 mg/g after 100 h, demonstrating that the proper PANI shell thickness coated on

the surface of Ag_3PO_4 particles could effectively prevent it from dissolution in the aqueous solution. Therefore, the proper PANI shell can significantly increase the structural stability of Ag_3PO_4 @PANI during the photocatalytic reaction. To assess the structural stability, we examined the crystalline structures of Ag_3PO_4 @PANI composite before and after the experiment. As shown in Fig. 11c, no extra characteristic diffraction peaks were observed in XRD spectra pattern of Ag_3PO_4 @PANI, which implied that there were no evident crystalline structure changes after the photocatalytic reaction. This result further confirmed that the PANI shell improved the stability of the Ag_3PO_4 photocatalyst, which was also confirmed by TEM of the composite sample after the reaction. For pure Ag_3PO_4 (Fig. 11d), after the photocatalytic recycles, the spherical particles disappeared, and web-like morphologies formed, indicating that the structure of the Ag_3PO_4 crystal was demolished. As for Ag_3PO_4 @PANI (Fig. 11e) after photocatalytic recycles under visible irradiation, it clearly showed that there was no formation of small Ag particles on the interface of Ag_3PO_4 with PANI. Therefore, the incorporation of PANI into Ag_3PO_4 photocatalyst not only enhanced the visible light photocatalytic performance of Ag_3PO_4 but also inhibited the photo-corrosion, thereby resulting in enhanced stability of photocatalytic activity.

To elucidate the photocatalytic reaction mechanism, we attempted to investigate the main reactive species including h^+ , $\cdot\text{O}_2^-$, and $\cdot\text{OH}$ involved in the photocatalytic process [50–52]. In

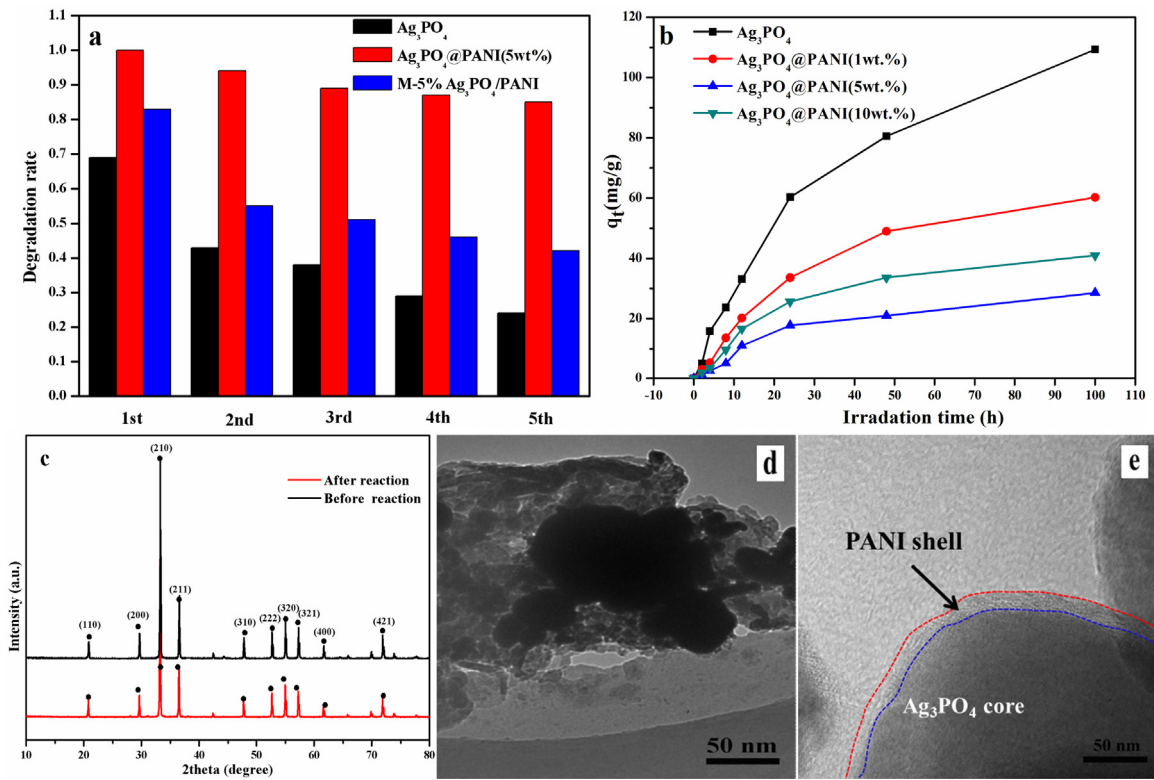


Fig. 11. Recycling runs (a) of the degradation of phenol, (b) ICP of Ag_3PO_4 and $\text{Ag}_3\text{PO}_4@\text{PANI}$ composite in water (c) before and after the photocatalytic reaction. (d,e) TEM images of photocatalysts before and after photocatalytic degradation of phenol under visible light irradiation.

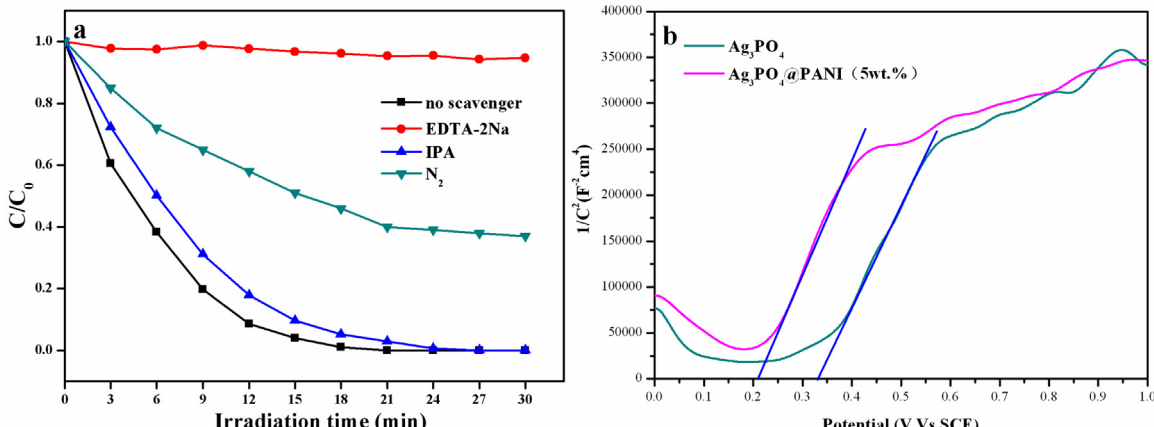


Fig. 12. (a) Plots of photogenerated active species trapped in the system of photodegradation of phenol by $\text{Ag}_3\text{PO}_4@\text{PANI}$ under visible light (b) Mott-Schottky (MS) plots of pure Ag_3PO_4 and $\text{Ag}_3\text{PO}_4@\text{PANI}$.

these experiments, EDTA-2Na, N₂, and isopropyl alcohol (IPA) were added to the photocatalytic reaction process as the scavengers for h⁺, •O₂⁻, and •OH, respectively. The detailed free radical capture experimental processes were similar to the photocatalytic experiments, and the results are shown in Fig. 12a. The results indicated that •OH was not the dominant active species in this process because the addition of isopropyl alcohol did not significantly inhibit the photocatalytic reaction. As depicted in Fig. 12a, the degradation rate decreased substantially to 5.36% in the presence of EDTA-2Na (h⁺ scavenger) while the degradation rate was 100% in the absence of scavengers, which suggested that h⁺ was the main reactive species for phenol degradation. Moreover, it could be seen that the photo-degradation process significantly decreased after N₂ was introduced and that the photo-degradation rate was

considerably reduced by approximately 63%. The results indicated that superoxide radicals and direct holes were active species for the photocatalytic degradation. The effect of PANI on the band edge potential of Ag_3PO_4 was investigated by Impedance Potential technique. As shown in Fig. 12b, the Mott-Schottky (MS) plots for Ag_3PO_4 and $\text{Ag}_3\text{PO}_4@\text{PANI}$ indicated they were typical n-type semiconductors with overall positive slopes. The flat-band potentials of Ag_3PO_4 and $\text{Ag}_3\text{PO}_4@\text{PANI}$, calculated from the x-intercepts of the linear region, were found to be 0.33 V and 0.21 V vs. SCE. It is well-known that the potential of the conduction band in the n-type semiconductor is more negative by 0.1 V than that of the flat band potential [53]. Hence, the conduction band potentials (ECB) of Ag_3PO_4 and $\text{Ag}_3\text{PO}_4@\text{PANI}$ were determined to be 0.23 V and 0.11 V vs. SCE (equivalent to 0.47 V and 0.35 V vs. NHE), respec-

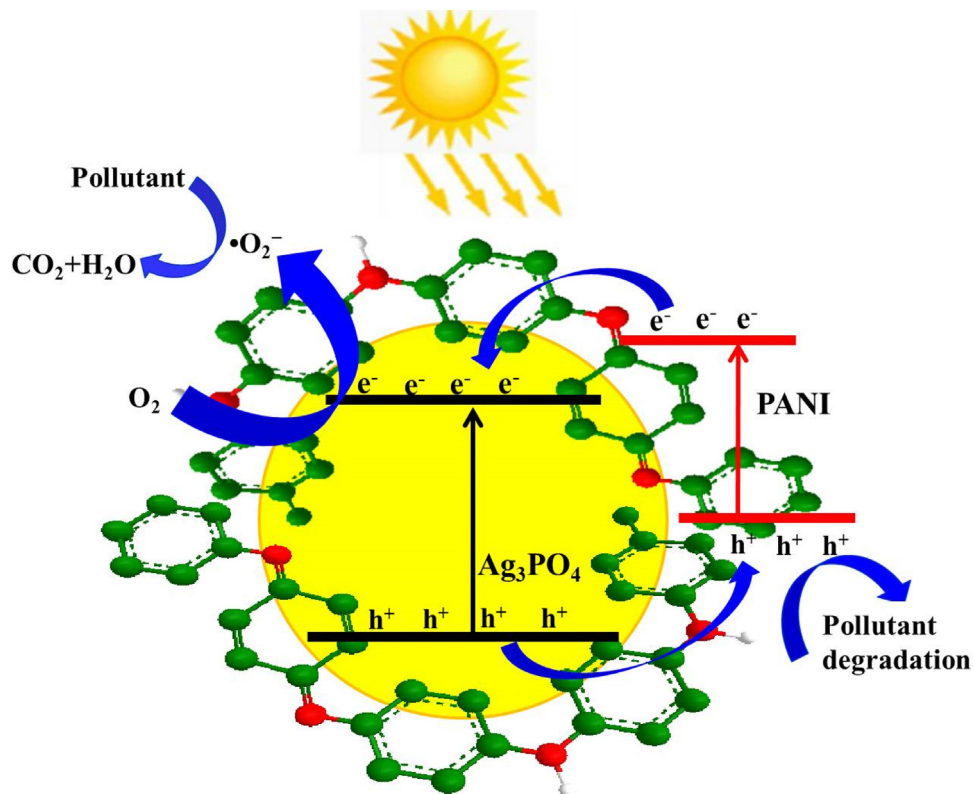


Fig. 13. Proposed photocatalytic mechanism for $\text{Ag}_3\text{PO}_4@\text{PANI}$ composite under visible-light illumination.

tively. Apparently, the ECB of $\text{Ag}_3\text{PO}_4@\text{PANI}$ composite showed a large negative shift of 0.12 V compared with that of pure Ag_3PO_4 . It could be inferred that the electronic interactions between PANI and Ag_3PO_4 caused a negative shift in the conduction band potential, which resulted in a highly positioned conduction band and a stronger reductive power for the $\text{Ag}_3\text{PO}_4@\text{PANI}$ composite.

On the basis of the above analysis, a possible mechanism for the degradation of phenol of $\text{Ag}_3\text{PO}_4@\text{PANI}$ composite under visible irradiation is proposed in Fig. 13. It is well known that both Ag_3PO_4 and PANI can be excited to generate electrons and holes under visible light irradiation. Photo-generated electrons and holes are generated on the HOMO and LUMO of PANI when irradiated by visible light. The LUMO and HOMO potentials of PANI are -2.1 and 1.3 eV, respectively, and CB and VB of Ag_3PO_4 are 0.47 and 2.92 eV, respectively [54,55]. Since the LUMO potential of PANI is more negative than CB of Ag_3PO_4 , the photo-generated electrons of PANI can be directly injected into the CB of Ag_3PO_4 through the well-defined interface, and then react with oxygen molecules to generate $\cdot\text{O}_2^-$ radicals [56]. Simultaneously, the excited holes produced by Ag_3PO_4 are injected into the HOMO of PANI. Furthermore, since the specific π -conjugated structure PANI is an excellent material for transporting holes, the holes can be transferred easily to the surface and oxidize the adsorbed contaminants directly, which contributes to the dramatically visible activity of $\text{Ag}_3\text{PO}_4@\text{PANI}$ photocatalyst in phenol degradation. As a result, the charge transfer efficiently inhibits the recombination of photo-generated electron-hole pairs, thereby enhancing the photocatalytic activity of $\text{Ag}_3\text{PO}_4@\text{PANI}$ photocatalyst.

4. Conclusion

In this work, $\text{Ag}_3\text{PO}_4@\text{PANI}$ photocatalyst with core@shell structure was prepared by a chemisorption method. The results of this study indicated that the introduction of PANI significantly

improved the visible-light responsive photocatalytic activity of the Ag_3PO_4 photocatalyst and the content of PANI dramatically affected the photocatalytic performance of $\text{Ag}_3\text{PO}_4@\text{PANI}$ composite. The photocatalytic activities for degradation of phenol and 2, 4-dichlorophenol over $\text{Ag}_3\text{PO}_4@\text{PANI}$ (5%) composite reached 100% and 95.3%, which were respectively 1.44 and 1.38 times of that of bulk Ag_3PO_4 . The activity of $\text{Ag}_3\text{PO}_4@\text{PANI}$ remained 85% after five cycling runs, whereas the activities of M- $\text{Ag}_3\text{PO}_4/\text{PANI}$ (5 wt.%) and Ag_3PO_4 only remained 42% and 24%, respectively, indicating that $\text{Ag}_3\text{PO}_4@\text{PANI}$ photocatalyst possessed a superior stability. The enhancement of photocatalytic performance and stability is mainly attributed to the superior charge mobility derived from the π -conjugated structure of PANI and to the efficient separation and transfer of photo-generated electron-hole at the interface between PANI and Ag_3PO_4 resulted from their matched energy level. In addition, PANI shell can prevent the dissolution of Ag_3PO_4 particles in aqueous solution during the photocatalytic reaction, leading to a high stability of the $\text{Ag}_3\text{PO}_4@\text{PANI}$ composite photocatalyst. In conclusion, $\text{Ag}_3\text{PO}_4@\text{PANI}$ composite is a promising photocatalyst for the removal and degradation of organic pollutants in the environment.

Acknowledgements

This work was financially supported by the National Natural Science Foundation of China (No. 51372068), Hebei Natural Science Funds for Distinguished Young Scholar (No. B2014209304), Key Program of Natural Science of Hebei Province (B2016209375). Li Liu and Lan Ding both contributed equally to this work, and the authors declare that they have no conflict of interest.

References

- [1] M.N. Chong, B. Jin, C.W.K. Chow, C. Saint, Water. Res. 44 (2010) 2997–3027.

- [2] R. Daghfir, P. Drogui, D. Robert, Ind. Eng. Chem. Res. 52 (2013) 3581–3599.
- [3] X.J. Wang, W.Y. Yang, F.T. Li, Y.B. Xue, R.H. Liu, Y.J. Hao, Ind. Eng. Chem. Res. 52 (2013) 17140–17150.
- [4] W.F. Shangguan, A. Yoshida, J. Phys. Chem. B 47 (2002) 12227–12230.
- [5] A. Kudo, K. Omori, H. Kato, J. Am. Chem. Soc. 49 (1999) 11459–11467.
- [6] J.W. Xu, Z.D. Gao, K. Han, Y.M. Liu, Y.Y. Song, ACS Appl. Mater. Interfaces. 6 (2014) 15122–15131.
- [7] G. MaX, B. Lu, D. Li, J. Phys. Chem. C 11 (2011) 4680–4687.
- [8] Z.G. Yi, J.H. Ye, N. Kikugawa, Nat. Mater. 7 (2010) 559–564.
- [9] C.T. Dinh, T.D. Nguyen, F. Kleitz, T.O. Do, Chem. Commun. 47 (2011) 7797–7799.
- [10] C. Cui, Y.P. Wang, D.Y. Liang, W. Cui, H.H. Hu, B.Q. Lu, S. Xu, X.Y. Li, C. Wang, Y. Yang, Appl. Catal. B: Environ. 158 (2014) 150–160.
- [11] J.H. Liu, X. Li, F. Liu, L.H. Lu, L. Xu, L.W. Liu, W. Chen, L.M. Duan, Z.R. Liu, Catal. Commun. 46 (2014) 138–141.
- [12] Y.H. Yan, H.Y. Guan, S. Liu, R.Y. Jiang, Ceram. Int. 40 (2014) 9095–9100.
- [13] J. Yan, C. Wang, H. Xu, Y.G. Xu, X.J. She, J.J. Chen, Y.H. Song, H.M. Li, Q. Zhang, Appl. Surf. Sci. 287 (2013) 178–186.
- [14] C. Jin, G.L. Liu, L.H. Zu, Y. Qin, J.H. Yang, J. Colloid Interface Sci. 453 (2015) 36–41.
- [15] L. Liu, Y.H. Qi, J.S. Hu, Y.H. Liang, W.Q. Cui, Appl. Surf. Sci. 351 (2015) 1146–1154.
- [16] S. Khanchandani, S. Kundu, A. Patra, A.K. Ganguli, J. Phys. Chem. C 116 (2012) 23653–23662.
- [17] D.M. Chen, K.W. Wang, D.G. Xiang, R.L. Zong, W.Q. Yao, Y.F. Zhu, Appl. Catal. B: Environ. 147 (2014) 554–567.
- [18] L. Liu, J.C. Liu, D.D. Sun, Catal. Sci. Technol. 2 (2012) 2525–2532.
- [19] J.Q. Li, H. Yuan, Z.F. Zhu, J. Colloid Interface Sci. 462 (2016) 382–388.
- [20] Y. Wang, X. Li, Y. Wang, C. Fan, J. Solid State Chem. 202 (2013) 51–56.
- [21] G. Yu, J. Gao, J.C. Hummelen, F. Wudl, A.J. Heeger, Science 270 (1995) 1789–1791.
- [22] S. Zhu, T. Xu, H. Fu, J. Zhao, Y. Zhu, Environ. Sci. Technol. 41 (2007) 6234–6239.
- [23] G. Williams, B. Seger, P.V. Kamat, ACS Nano 2 (2008) 1487–1491.
- [24] X.C. Wang, S. Blechert, M. Antonietti, ACS Catal. 2 (2012) 1596–1606.
- [25] J. Wang, X.Y. Ni, Solid State Commun. 146 (2008) 239–344.
- [26] L. Liu, Y.H. Qi, J.L. Lu, S.L. Lin, W.J. An, Y.H. Liang, W.Q. Cui, Appl. Catal. B: Environ. 183 (2016) 133–141.
- [27] X. Li, G. Wang, X. Li, D. Lu, Appl. Surf. Sci. 229 (2004) 395–401.
- [28] M. Nandi, R. Gangopadhyay, A. Bhaumik, Microporous Mesoporous Mater. 109 (2008) 239–247.
- [29] H. Zhang, R.L. Zong, Y.F. Zhu, J. Phys. Chem. C. 113 (2009) 4605–4611.
- [30] C. Wang, L. Wang, J. Jin, J. Liu, Y. Li, M. Wu, L.H. Chen, B.J. Wang, X.Y. Yang, B.L. Su, Appl. Catal. B: Environ. 188 (2016) 351–359.
- [31] Y.Y. Bu, Z.Y. Chen, ACS Appl. Mater. Interfaces 6 (2014) 17589–17598.
- [32] B.J. Jiang, Y.H. Wang, J.Q. Wang, C.G. Tian, W.J. Li, Q.M. Feng, Q.J. Pan, H.G. Fu, ChemCatChem 5 (2013) 1359–1367.
- [33] J.F. Ma, Q. Liu, L.F. Zhu, J. Zou, K. Wang, M.R. Yang, S. Komarneni, Appl. Catal. B: Environ. 182 (2016) 26–32.
- [34] C. Cui, Y.P. Wang, D.Y. Liang, W. Cui, H.H. Hu, B.Q. Lu, S. Xu, X.Y. Li, C. Wang, Y. Yang, Appl. Catal. B: Environ. 158–159 (2014) 150–160.
- [35] P.Y. Dong, Y.H. Wang, H.H. Li, H. Li, X.L. Ma, L.L. Han, J. Mater. Chem. A 1 (2013) 4651–4656.
- [36] Z.L. Xiu, H. Bo, Y.Z. Wu, X.P. Hao, Appl. Surf. Sci. 289 (2014) 394–399.
- [37] M. Thomas, S.K. Ghosh, K.C. George, Mater. Lett. 56 (2002) 386–392.
- [38] N. Umezawa, S.X. Ouyang, J.H. Ye, J. Phys. Rev. B 83 (2011) 1–8.
- [39] H. Zhang, Y.F. Zhu, J. Phys. Chem. C 114 (2010) 5822–5826.
- [40] H. Zhang, R.L. Zong, J.C. Zhao, Y.F. Zhu, Environ. Sci. Technol. 42 (2008) 3803–3807.
- [41] P.Y. Dong, Y.H. Wang, B.C. Cao, S.Y. Xin, L.N. Guo, J. Zhang, F.H. Li, Appl. Catal. B: Environ. 131–133 (2013) 45–53.
- [42] J.T. Feng, Y.H. Hou, X.Y. Wang, W.L. Quan, J.M. Zhang, Y.C. Wang, L.C. Li, J. Alloys Compd. 681 (2016) 157–166.
- [43] D.P. Wang, H.C. Zeng, J. Phys. Chem. C 113 (2009) 8097–8106.
- [44] M.T. Greiner, M.G. Helander, W.M. Tang, Z.B. Wang, J. Qiu, Z.H. Lu, Nat. Mater. 11 (2012) 79–81.
- [45] H. Zhang, G. Wang, D. Chen, X.J. Lv, J.H. Li, Chem. Mater. 20 (2008) 6543–6549.
- [46] Y.H. Liang, S.L. Lin, L. Liu, J.S. Hu, W.Q. Cui, Appl. Catal. B: Environ. 164 (2015) 192–203.
- [47] Y.Y. Bu, Z.Y. Chen, C.J. Sun, Appl. Catal. B: Environ. 179 (2015) 363–371.
- [48] X.J. Chen, Y.Z. Dai, X.Y. Wang, J. Guo, T.H. Liu, F.F. Li, J. Hazard. Mater. 292 (2015) 9–18.
- [49] W.J. Jiang, Y.F. Liu, J. Wang, M. Zhang, W.J. Luo, Y.F. Zhu, Adv. Mater. Interfaces (2015) 1500502.
- [50] M.C. Yin, Z.S. Li, J.H. Kou, Z.G. Zou, Environ. Sci. Technol. 43 (2009) 8361–8366.
- [51] Z.G. Zou, J.H. Ye, K. Sayama, H. Arakawa, Lett. Nat. 414 (2001) 625–627.
- [52] Y.L. Li, Y.M. Liu, J.S. Wang, E. Uchaker, Q.F. Zhang, S.B. Sun, Y.X. Huang, J.Y. Li, G.Z. Cao, J. Mater. Chem. A 1 (2013) 7949–7956.
- [53] A. Ishikawa, T. Takata, J.N. Kondo, M. Hara, H. Kobayashi, J. Am. Chem. Soc. 124 (2002) 13547–13553.
- [54] W.M. Wu, S.J. Liang, L.J. Shen, Z.X. Ding, H.R. Zheng, W.Y. Su, L. Wu, J. Alloys Compd. 520 (2012) 213–219.
- [55] X.F. Yang, H.Y. Cui, Y. Li, J.L. Qin, R.X. Zhang, H. Tang, ACS Catal. 3 (2013) 363–369.
- [56] J.F. Ma, Q. Liu, L.F. Zhu, J. Zou, K. Wang, M.R. Yang, S. Komarneni, Appl. Catal. B: Environ. 182 (2016) 26–32.